Supporting Information for

Benzotriazole-based Ionic COFs Embedded in Biologic Aerogels for Stable Photocatalytic Seawater Splitting

Ting Wang,[acd] Mingjie Li*[b], Jiajun Huang,[c] Renqiang Yang*[a] and Chaoxu Li*[a]

[a]*Key Laboratory of Flexible Optoelectronic Materials and Technology (Ministry of Education), School of Optoelectronic Materials & Technology, Jianghan University, Wuhan 430056, China*

[b]*Key Laboratory of Rubber-Plastics, Ministry of Education/Shandong Provincial Key Laboratory of Rubber-plastics, State Key Laboratory of Advanced Optical Polymer and Manufacturing Technology, Qingdao University of Science & Technology, Zhengzhou Road 53, Qingdao, 266042, China*

[c]*Qingdao Institute of Bioenergy and Bioprocess Technology, Chinese Academy of Sciences, 189 Songling Road, Qingdao 266101, China*

[d]*Hubei Three Gorges Laboratory, 1 Mazongling Road, Yichang, 443007, China*

Chemicals. Dibromoethane, triformylpholoroglucinol (Tp) and sodium hydride were purchased from Anhui Zesheng Technology Co. Ltd. 4-aminophenylboronic acid pinacol ester, ascorbic acid (AA), hexachloroplatinic acid, azobisisobutyronitrile, cysteamine hydrochloride, anhydrous *N*,*N*-dimethyl formamide, 1,4-dioxane, *n*-butanol and *o*-dichlorobenzene were obtained from J&K scientific Co., Ltd, Shanghai Dibai Biological Technology Co. Ltd, or Macklin Biochemical Co., Ltd. All these commercial chemicals are analytical reagents and were directly used without further purification.

Millipore water (electric resistivity ~18.2 MΩ cm) was used as solvent and for H_2 evolution.

Characterization

^{1}H NMR and ^{13}C NMR spectra were recorded on a Bruker AVANCE-III 600 MHz spectrometer, with tetramethylsilane (TMS) as the internal standard. Solid-state cross-polarization magic angle spinning (CP/MAS) ^{13}C NMR spectra were acquired using a Bruker AVANCE NEO 500 MHz spectrometer at 25 °C. Fourier transform infrared (FT-IR) spectra were obtained on a Thermo Fisher Nicolet 6700 FT-IR spectrometer over a wavenumber range of 400−4000 cm^{-1}. X-ray photoelectron spectra (XPS) and ultraviolet photoelectron spectroscopy (UPS) were performed on a Thermo Scientific ESCALAB 250Xi X-ray photoelectron spectrometer, employing monochromatic Al Kα radiation (1486.6 eV) as the excitation source. Powder X-ray diffraction (PXRD) patterns were collected with an X-ray diffractometer (Bruker D8 ADVANCE) using Cu Kα radiation (λ = 1.5406 Å) with a scan rate of 1° min^{-1}. Thermal gravimetric analysis (TGA) and differential scanning calorimetry were conducted on a Ulvac TGD 9600 under nitrogen purge at a flow rate of 40 mL min^{-1} from room temperature to 800 °C at the ramp rate of 10 °C min^{-1}. The specific surface areas and porous structure of the samples were determined via the Brunauer-Emmett-Teller (BET) method and nolinear density functional theory (NLDFT), respectively, using a Quantachrome Autosorb iQ surface analyzer at 77 K under a relative N_2 pressure range from 0.05 to 1.00. Materials Studio software package was utilized for the simulation and refinement to confirm the molecular stacking mode. Ultraviolet-visible (UV-Vis) diffuse

reflectance spectra (DRS) were recorded in the range of 400−800 nm using a U-4100 spectrophotometer (Hitachi, Japan). Steady-state photoluminescence (PL) spectra were collected with a Hitachi F-7000 fluorescence spectrophotometer, while the dynamics of fluorescence decay were measured by using the time-correlated single-photon counting spectrophotometer (Nanolog, Horiba Scientific).

Morphologies characterization was performed via field-emission scanning electron microscopy (FESEM, Hitachi S-4800, Japan) at an acceleration voltage of 10 kV. For transmission electron microscopy (TEM) analysis, samples were prepared by pipetting ethanol-based dispersions onto ultrathin carbon-coated copper grids, followed by drying under ambient conditions. High-resolution transmission electron microscopy (HRTEM, JEOL JEM-F200, Japan) operating at 200 kV was used to visualize the lattice structures.

Electrical measurements

Electrical measurements were conducted on a CHI660E electrochemical workstation (CH Instrument, Shanghai, China) at room temperature with a three-electrode system using Ag/AgCl as the reference electrode and a platinum foil as the counter electrode in Na_2SO_4 electrolyte (0.2 M). Typically, 1.0 mg COFs and 20 μL of Nafion solution (5 wt%, Dupont) were added in 180 μL ethanol, followed by bath ultrasonication (45 Hz; 300 W) for 20 min. The mixture suspension was uniformly dropped onto the surface of polished glass carbon electrode (mass loading: ~0.5 mg cm^{-1}, 0.07 cm^{-2}), serving as working electrodes after fully dried at 25 °C. The measured potentials (*vs*. Ag/AgCl) should be converted to normal hydrogen electrode (NHE) scale *via* E (*vs*. NHE) = E (*vs*. Ag/AgCl) + 0.197 V. The electrochemical impedance spectroscopy (EIS, Nyquist plot) was carried out at the open-circuit potential within a frequency range from 10^5 to 0.1 Hz with 10 mV perturbation. The potential static *i-t* technique was used to collect the photocurrent at open circuit potential (OCP) with periodic light irradiation (300 W Xe-lamp, AM 1.5 with >420 nm filter).

Theoretical calculation

To obtain the electrostatic potential (ESP) surface**,** density functional theory (DFT) calculations were performed using Gaussian 09 software with the 6-31G (*d, p*) basis

set. The ground-state geometries were optimized using the popular B3LYP exchange-correlation functional, and the ESP analysis was carried out using the wavefunction analysis tool Multiwfn.

The water affinity and Gibbs free energy barrier along the photocatalytic pathway were calculated with D3 dispersion correction, as implemented in the CP2K software. The Perdew-Burke-Ernzerhof (PBE) functional was used for static electronic structure calculations and geometry optimizations. Input files for CP2K were prepared with the aid of the Multiwfn tool,[1] and DZVP-MOLOPT-GTH basis set was adopted. Due to the complexity of the current system, the K point was set to 1×1×1, and the SCF threshold was set to 1E-6 Ha. The adsorption energy between the COF monolayer and absorption molecules A [H_2O, H, H-OH and H_2] was evaluated using the following equation:

$$\Delta E_{\text{absorption}} = E(\text{COF} + \text{A}) - E(\text{COF}) \quad \text{(S1)}$$

The reaction energy gap was calculated as follows:

$$\Delta E_{\text{reaction}} = E(\text{COF} + \text{A}) - E(\text{COF} + \text{H}_2\text{O}) \quad \text{(S2)}$$

Solar evaporation experiments

In a typical experiment, a piece of hybrid aerogel (with an area of 1.8 cm^2) was floated in a flask containing 20 mL deionized water. Subsequently, the evaporator was placed under a solar simulator (300 W Xe lamp with a cut-420 nm filter) with a power density of 100 mW cm^{-2}. The solar flux was quantified using a power meter, while the mass loss of the system was monitored in real time with a high-precision electronic balance.

The surface temperature of the composite aerogel was mapped across the entire surface of the evaporator using an infrared camera. All experiments were conducted under controlled laboratory conditions, with the ambient temperature maintained at 25 °C and the relative air humidity stabilized at approximately 45%.

Photocatalysis experiments

The photocatalytic performance of the aerogels was evaluated in a hermetic quartz reactor equipped with a circulating water device, to maintain the reactor temperature at

approximately 15 °C. Typically, a piece of hybrid aerogel (with an area of 1.8 cm^2) was suspended in water (20 mL). The hydrogen evolution reaction was carried out using a xenon lamp (300 W, a cut-420 nm filter) as the simulated light source, ascorbic acid as the sacrificial gent and H_2PtCl_6 as the cocatalyst. Prior to the formal reaction, the system was irradiated for 30 min to initially deposit Pt particles onto the catalyst surface. The amount of generated H_2 was quantified using gas chromatography fitted with a thermal conductivity detector (TCD), using argon as the carrier gas.

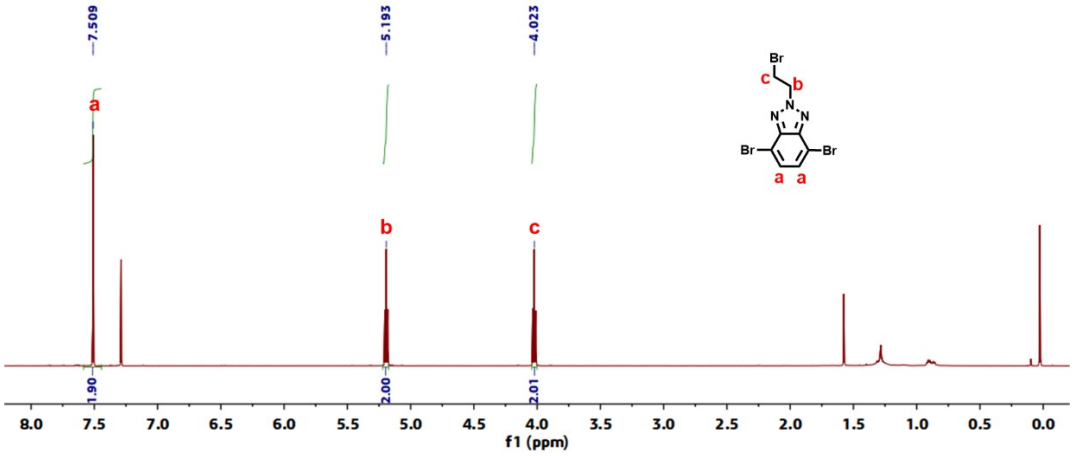

Figure S1. ^{1}H NMR spectrum of BTz-2Br.

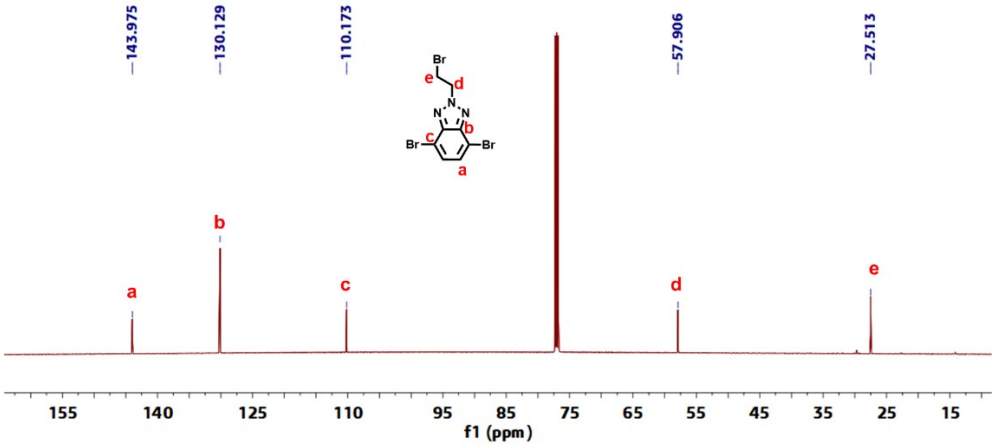

Figure S2. ^{13}C NMR spectrum of BTz-2Br.

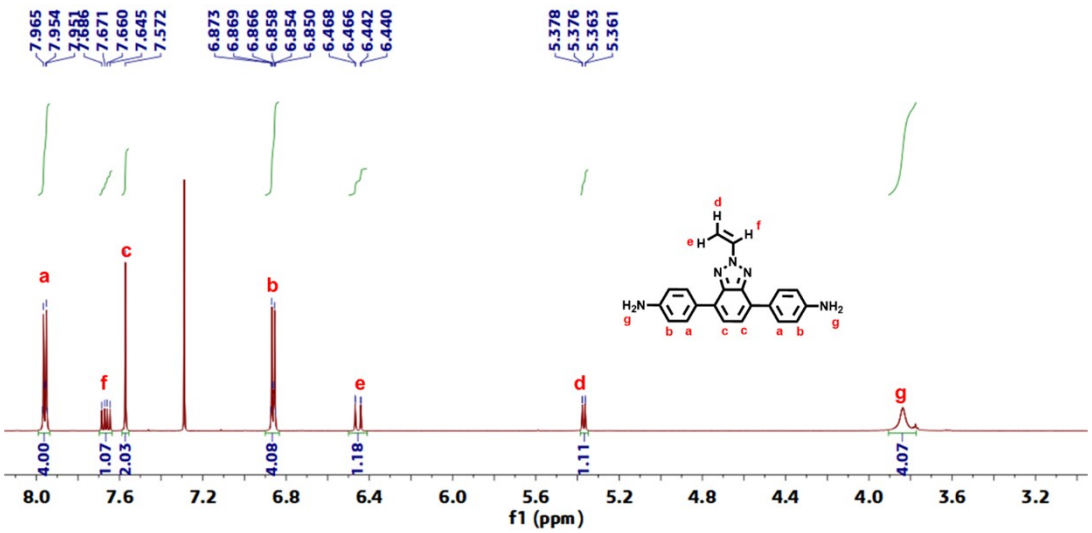

Figure S3. ^{1}H NMR spectrum of BTz-2NH$_2$.

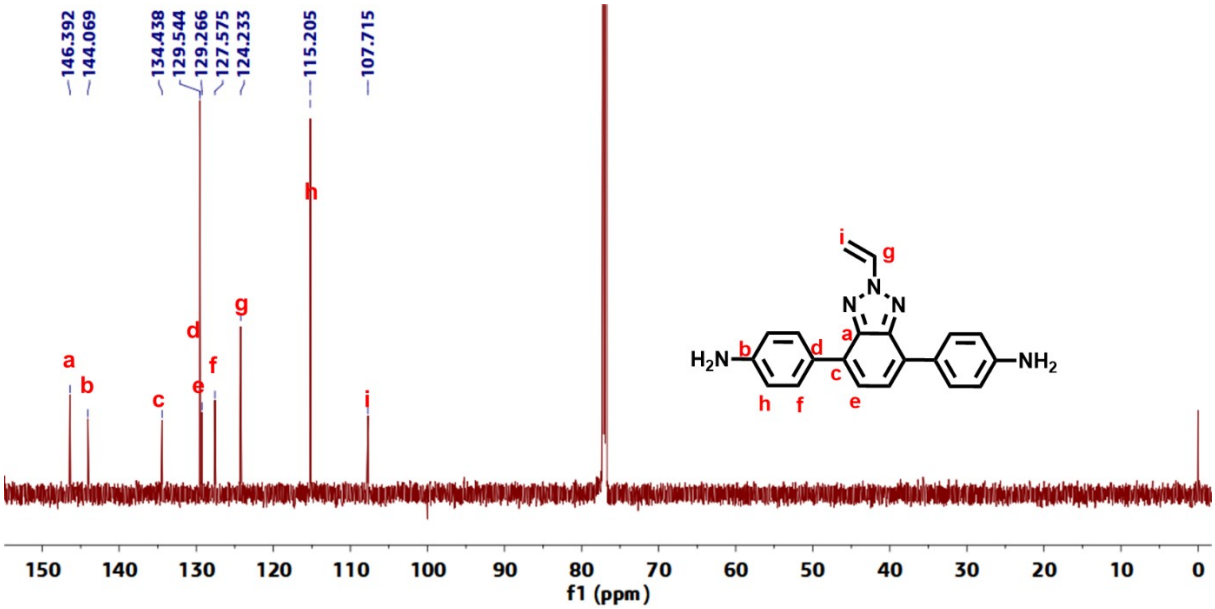

Figure S4. ^{13}C NMR spectrum of BTz-2NH$_2$.

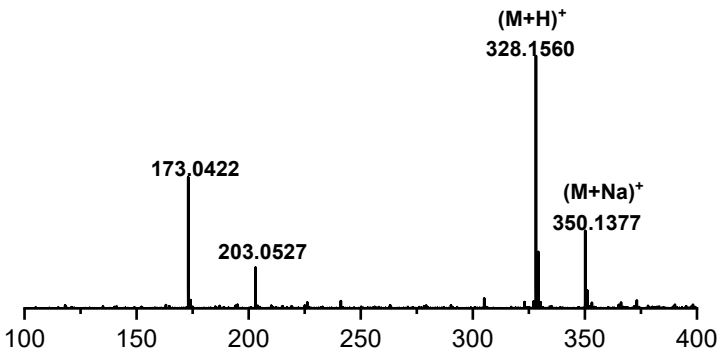

Figure S5. Mass spectrum of BTz-2NH$_2$.

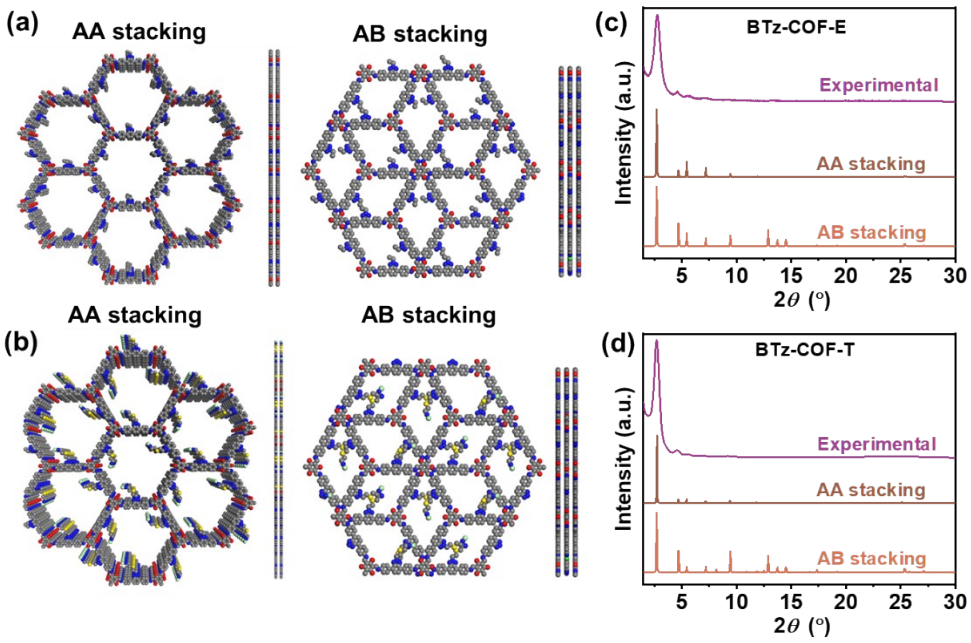

Figure S6. Structural analysis and PXRD patterns of BTz-COF-E and BTz-COF-T. (a & b) Structural model for AA stacking and AB stacking configurations of BTz-COF-E (a) and BTz-COF-T (b). (c & d) experimental PXRD patterns alongside with simulated diffraction patterns for AA stacking and AB stacking configurations of BTz-COF-E (c) and BTz-COF-T (d).

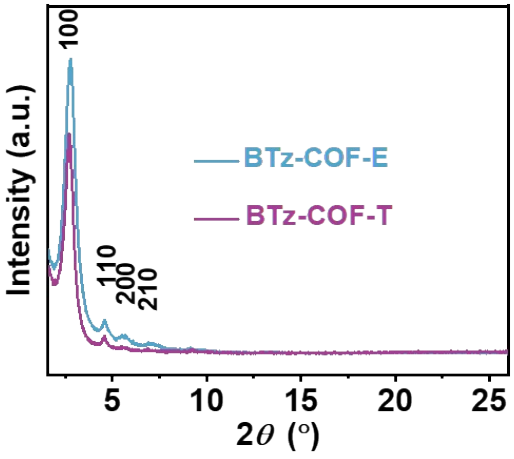

Figure S7. The comparison of PXRD patterns for BTz-COF-E and BTz-COF-T.

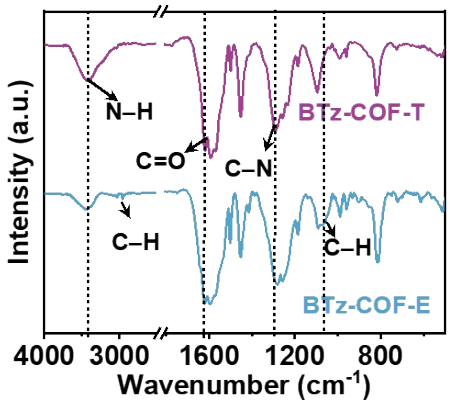

Figure S8. Comparison of the FT-IR spectra of BTz-COF-E and BTz-COF-T.

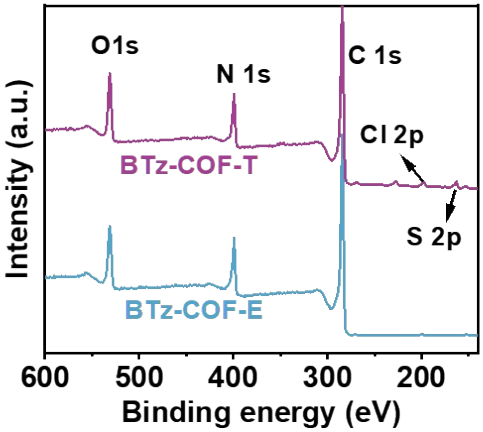

Figure S9. Typical XPS survey spectra of BTz-COF-E and BTz-COF-T.

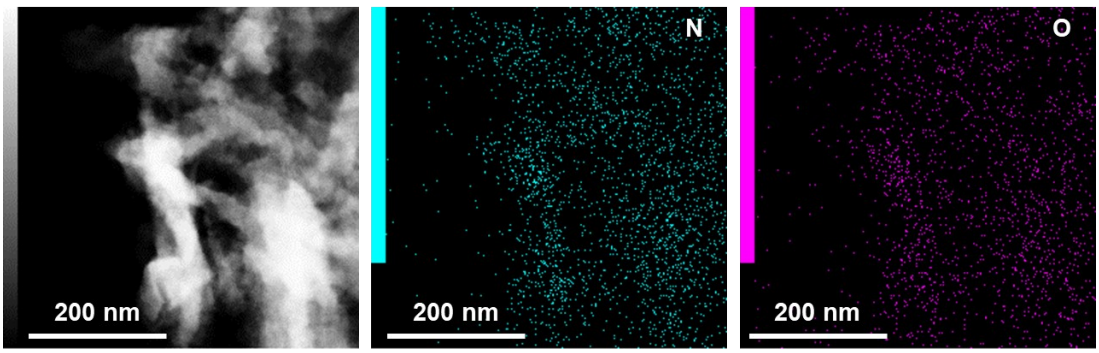

Figure S10. The element mapping images of BTz-COF-E.

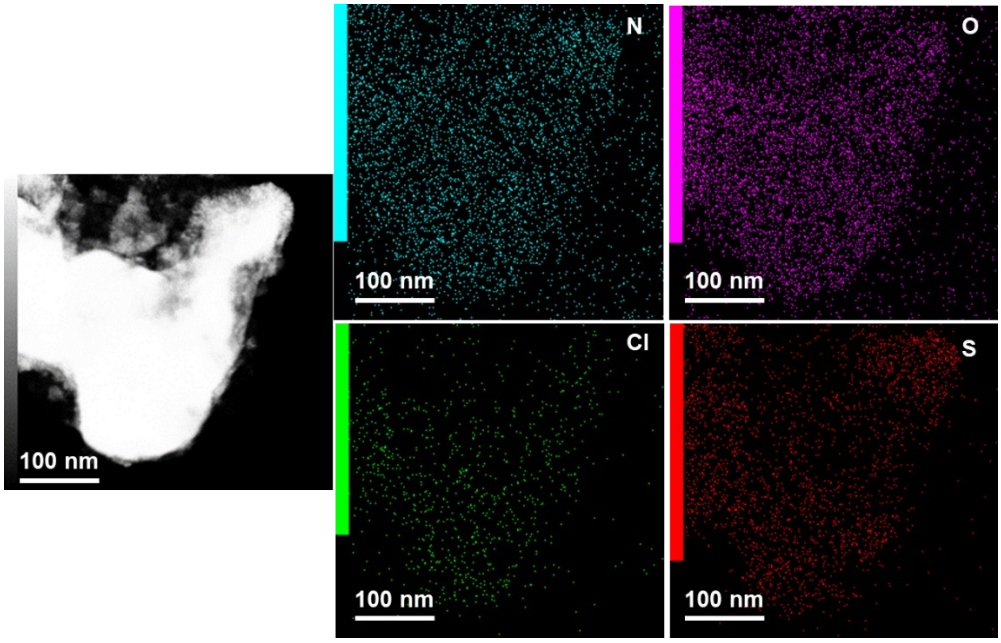

Figure S11. The element mapping images of BTz-COF-T.

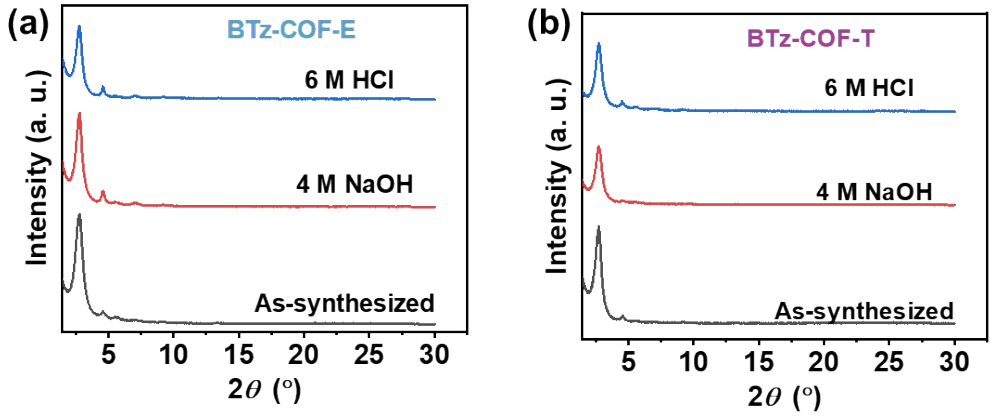

Figure S12. PXRD profiles of (a) BTz-COF-E and (b) BTz-COF-E, as-synthesized and after treating with 4 M NaOH and 6 M HCl for 24 h.

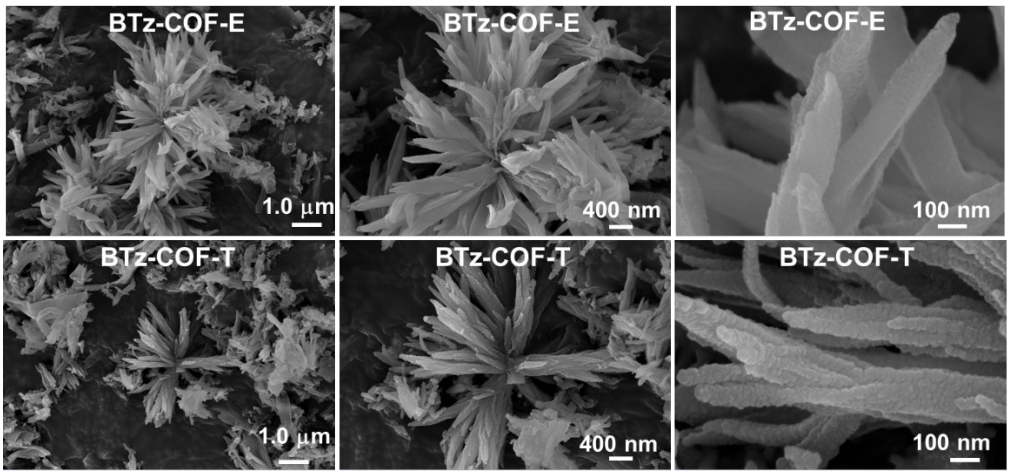

Figure S13. SEM images of BTz-COF-E and BTz-COF-T.

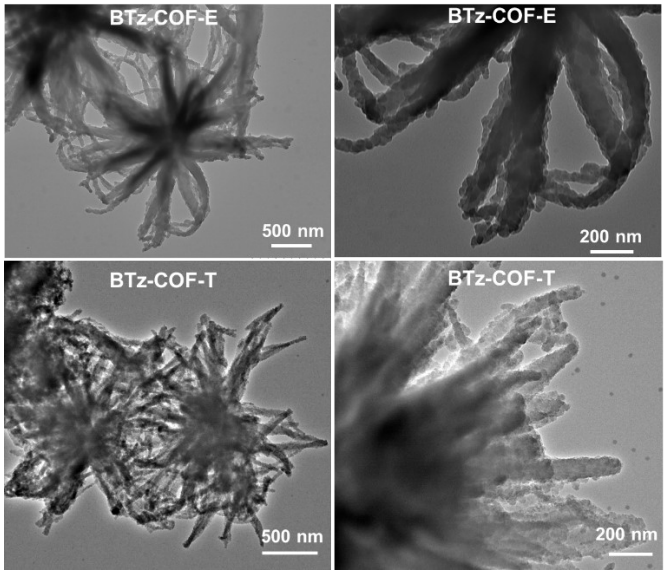

Figure S14. TEM images of BTz-COF-E and BTz-COF-T.

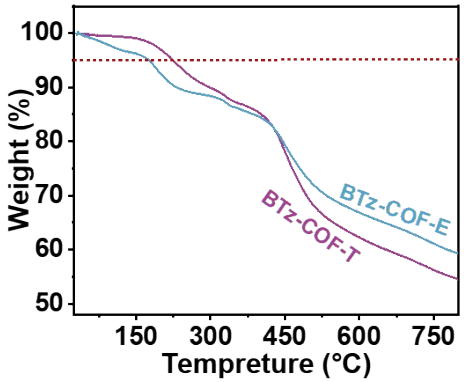

Figure S15. TGA curves of BTz-COF-E and BTz-COF-T recorded in nitrogen

atmosphere.

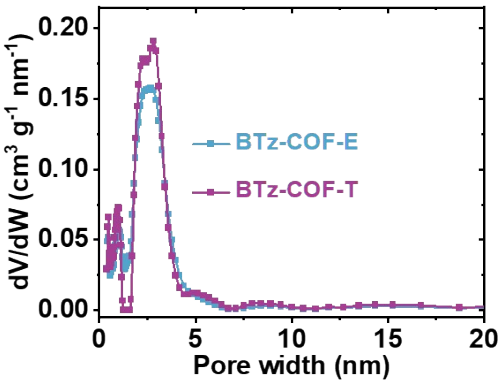

Figure S16. The pore size distributions profiles of BTz-COF-E and BTz-COF-T.

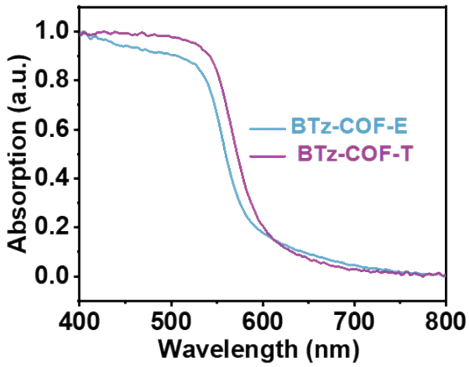

Figure S17. UV–vis DRS pattern of BTz-COF-E and BTz-COF-T.

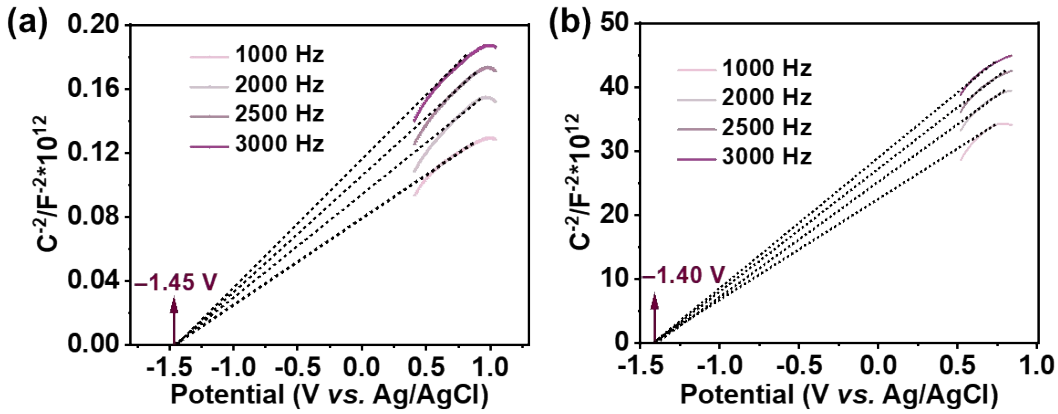

Figure S18. Mott–Schottky plots of BTz-COF-E (a) and BTz-COF-T (b).

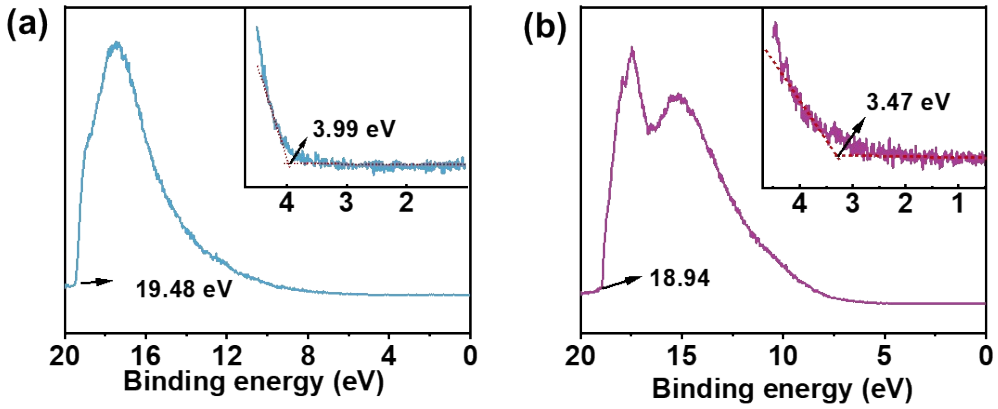

Figure S19. UPS spectra for BTz-COF-E (a) and BTz-COF-T (b).

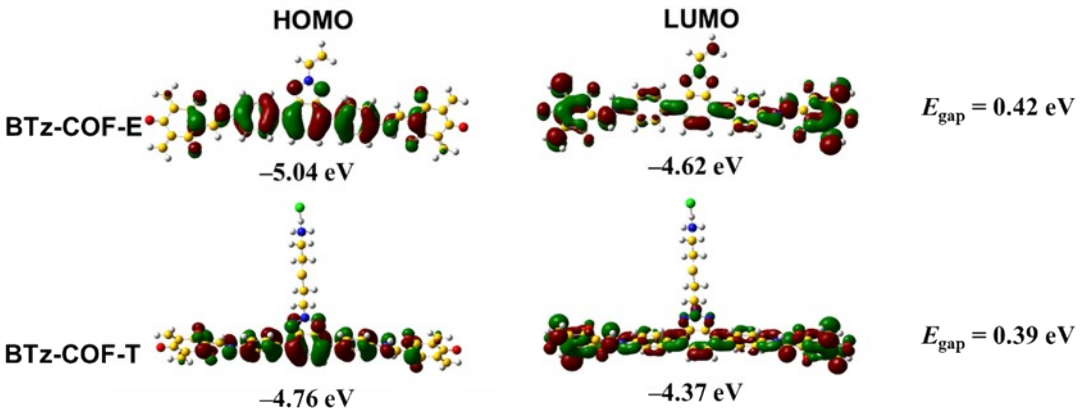

Figure S20. Calculated highest occupied molecular orbital (HOMO) and lowest unoccupied molecular orbital (LUMO) energy levels of BTz-COF-E and BTz-COF-T.

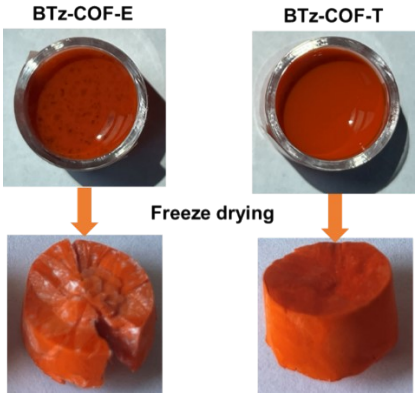

Figure S21. Digital pictures of the hybrid suspensions and the resulted aerogels.

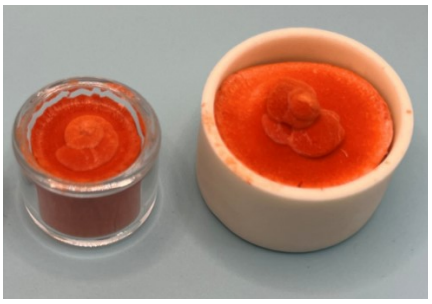

Figure S22. BTz-COF-T@CNF aerogels prepared using molds of different sizes.

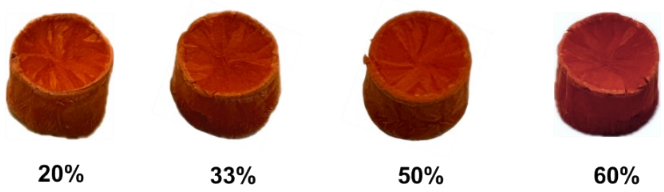

Figure S23. Digital photographs of hybrid aerogels with different COF mass ratios.

Figure S24. Digital photographs of BTz-COF-T@CNF (with COF mass ratio of 50%) on a dandelion.

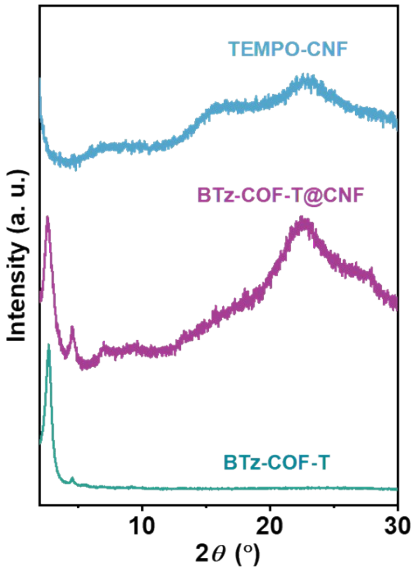

Figure S25. PXRD results of TEMPO-CNF, BTz-COF-T and BTz-COF-T@CNF aerogel.

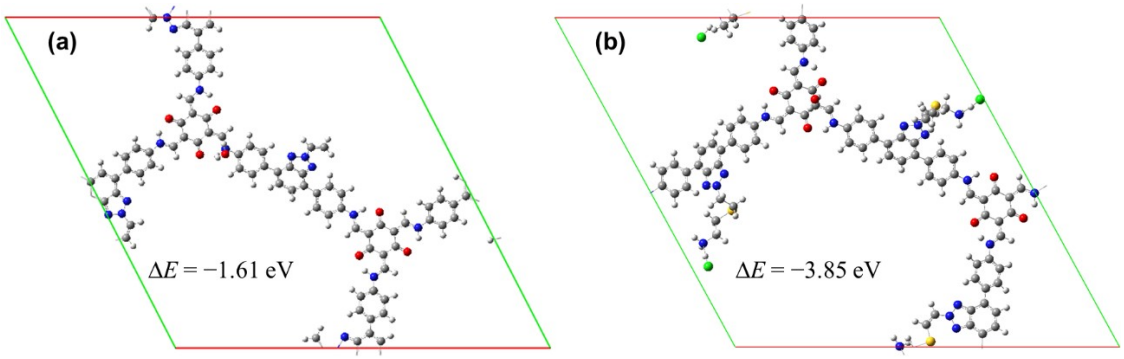

Figure S26. The simulated water affinity of (a) BTz-COF-E and (b) BTz-COF-T.

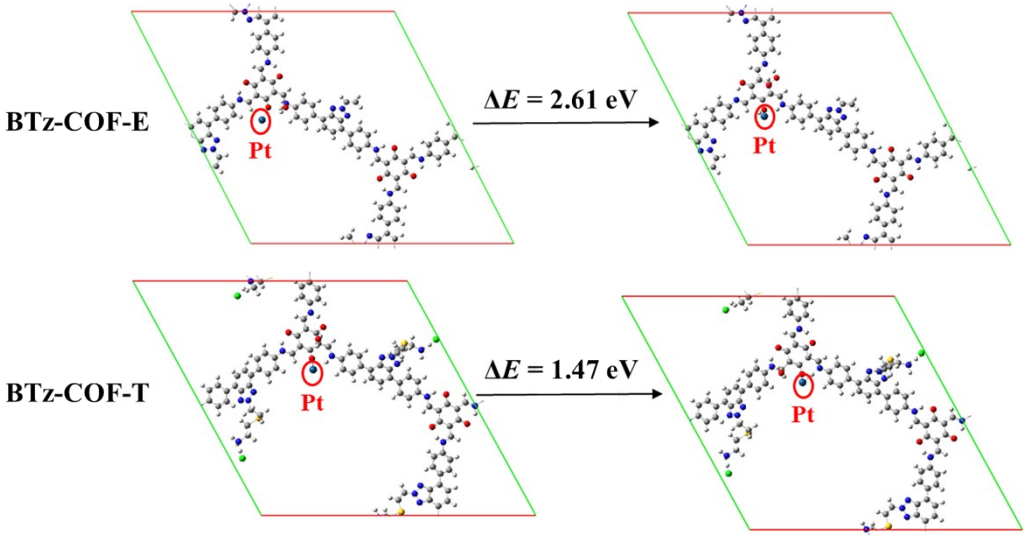

Figure S27. DFT-calculated Gibbs free energy changes (ΔE) for the water activation step ($H_2O \rightarrow$ H-OH*) on Pt sites supported by BTz-COF-E and BTz-COF-T.

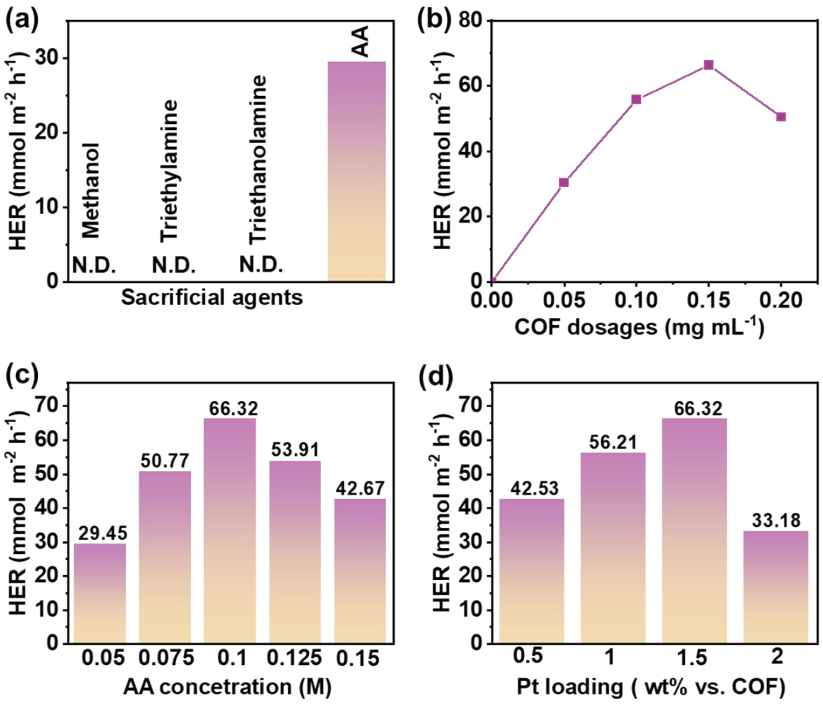

Figure S28. Dependence of H_2 evolution performances of BTz-COF-T@CNF on different (a) sacrificial agent species, (b) BTz-COF-T dosages, (c) AA concentration s and (d) Pt loading amounts. Experimental conditions: 50 mL H_2O, $\lambda \geq 420$ nm light irradiation (100 mW cm^{-2}).

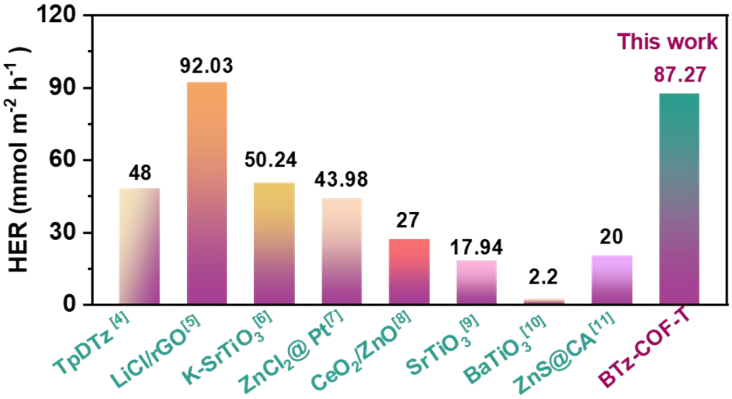

Figure S29. Comparison of HER of BTz-COF-T@CNF in seawater with classical reported semi-conductors performed in pure water.

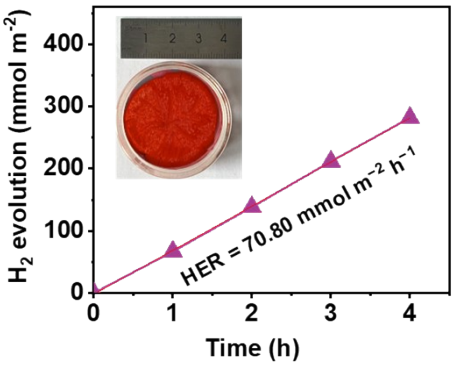

Figure S30. Photocatalytic H_2 evolution rate curves of the larger-area BTz-COF-T@CNF aerogel (9.62 cm^2). The top-left inset gives the optical image of the aerogel.

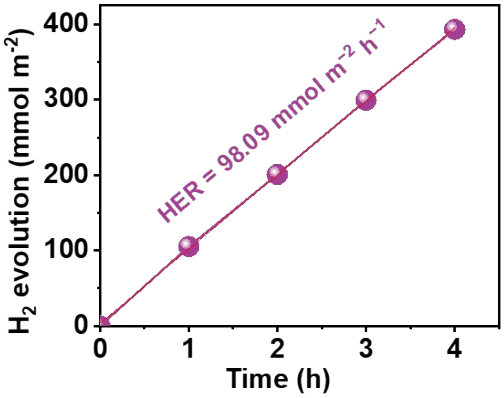

Figure S31. Photocatalytic H_2 production curves of BTz-COF-T@CNF in deionized water.

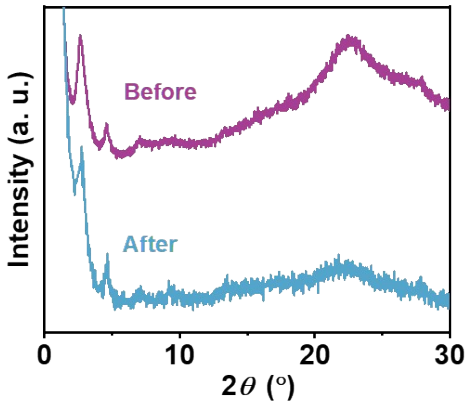

Figure S32. Comparison of PXRD before and after photocatalytic process for BTz-COF-T@CNF.

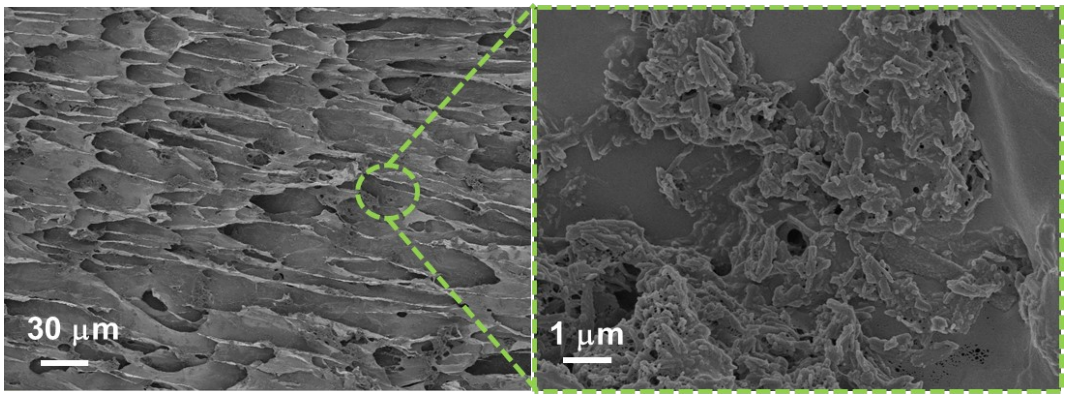

Figure S33. SEM images for BTz-COF-T@CNF after photocatalysis.

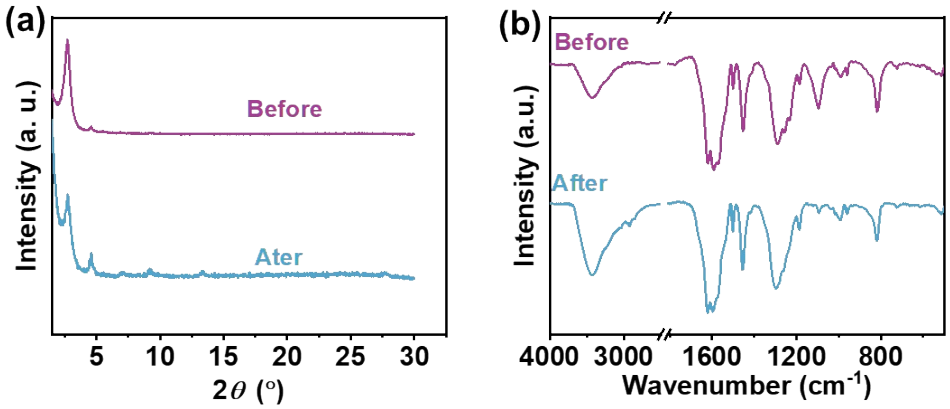

Figure S34. Comparison of (a) PXRD and (b) FT-IR before and after photocatalytic process for BTz-COF-T.

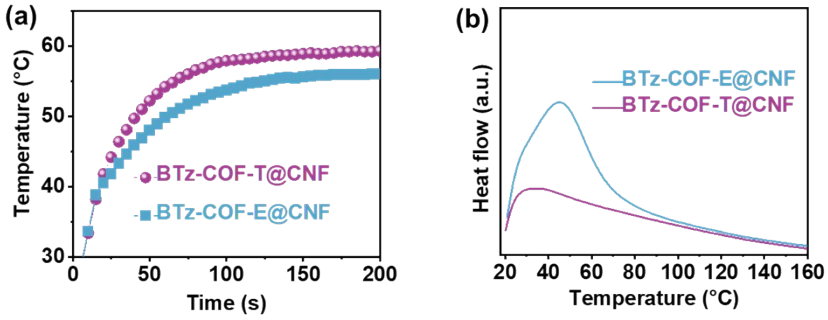

Figure S35. (a) Temperature change with time of BTz-COFs-based aerogels in water. (b) DSC curves of hydrated BTz-COF-E@CNF and hydrated BTz-COF-T@CNF. Under 1 sun irradiation, the surface temperature of BTz-COF-E@CNF aerogel balanced at 53.1 °C, while the BTz-COF-T@CNF aerogel could reach a maximum temperature of 57.4 °C, clearly indicating a superior light-to-thermal conversion efficiency. Moreover, differential scanning calorimetry revealed that BTz-COF-T@CNF exhibited a lower phase transition temperature and a smaller equivalent

evaporation enthalpy.

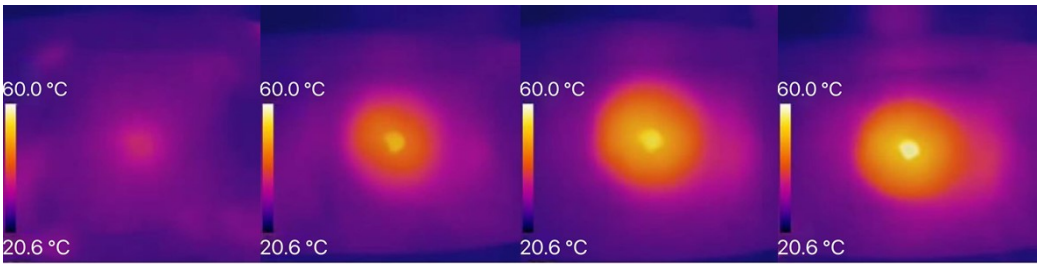

Figure S36. Infrared images of temperature variation of BTz-COF-T@CNF aerogel under different irradiation time under 1 sunlight.

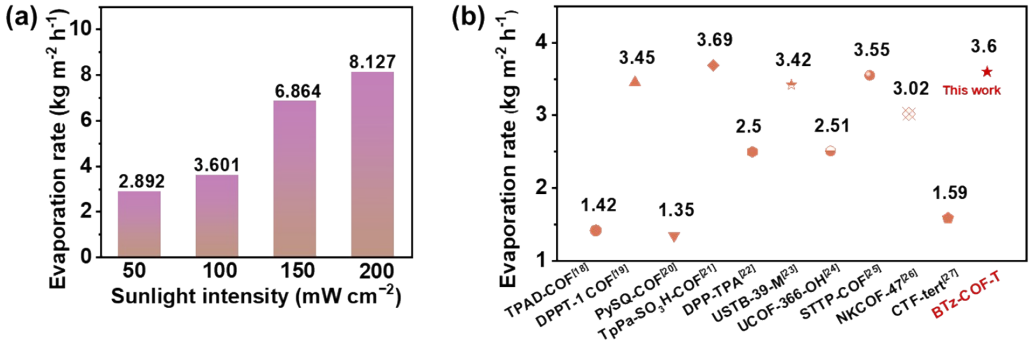

Figure S37. (a) Evaporation rates of BTz-COF-T@CNF under different solar irradiation intensities. (b) Comparison of water evaporation rates of BTz-COF-T@CNF with some reported COF-based evaporators.

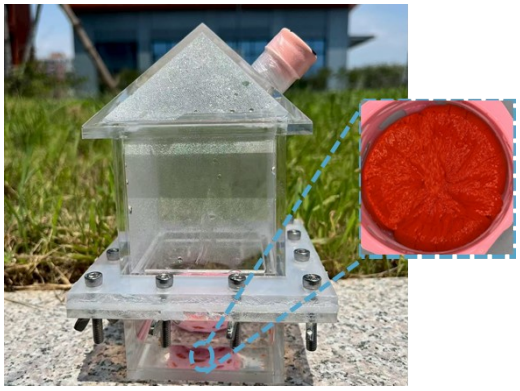

Figure S38. The equipment and the BTz-COF-T@CNF aerogel in seawater for the photothermal-assisted photocatalysis experiments.

Table S1. Comparison of photocatalytic performance of BTz-COF-T@CNF with other reported materials.

Photocatalyst	Cocatalyst	Sacrificial agent	Light source	HER ($mmol\ m^{-2}\ h^{-1}$)	Ref
TpDTz	Pt	Ascorbic acid	300 W Xe lamp (>420 nm) 170 mW cm^{-2}	48	2
LiCl/rGO/Nv-CN/Ov-BVO	—	—	100 mW cm^{-2}	92.03	3
K-$SrTiO_3$-loaded TiN	Co	—	300 W Xe lamp (>300 nm) 100 mW cm^{-2}	50.24	4
$ZnCl_2$@ Pt	Pt	—	AM 1.5G 100 mW cm^{-2}	43.98	5
CeO_2/ZnO nanotube	—	Na_2SO_3	300 W Xe lamp 100 mW cm^{-2}	27	6
$SrTiO_3$	—	—	500 W Xe lamp 100 mW cm^{-2}	17.94	7
Polydopamine-$BaTiO_3$/$CuPbSbS_3$	Pt	Methanol	100 mW cm^{-2}	2.2	8
ZnS@CA	—	Methanol	LED lamp (>420 nm) 60 mW cm^{-2}	20	9
BTz-COF-T@CNF	Pt	Ascorbic acid	300 W Xe lamp 100 mW cm^{-2}	87.27	**This work**

Table S2. Comparison of apparent quantum efficiency (AQE) of BTz-COF-T with other semiconductor photocatalysts.

Photocatalysts	**Wavelength**	**AQE**	**Sacrificial agent**	**Year**	**Ref**
TpPa COF	420	8.6	Ascorbic acid	2026	10
TPBD COF	420	1.9	Ascorbic acid	2025	11
	450	3.6			
FO@SO/ZIS	420	4.5	Triethanolamine	2023	12
g-C_3N_4 Com	420	13.1	Triethanolamine	2018	13
CDs/CdS	420	11.8	Lactic acid	2019	14
ZIS/PAN	420	1.5	Triethanolamine	2024	15
CDs/TCN	420	7.8	Triethanolamine	2023	16
COP-TF@CNi_2P	400	2.5	Na_2S & Na_2SO_3	2019	17
BTz-COF-T	420	11.6	Ascorbic acid		This work

Table S3. Comparison of evaporation performance with COFs-based solar absorbers.

Evaporator	**Matrix/substrate**	**Water evaporation rate ($kg\ m^{-2}\ h^{-1}$)**	**Ref**
TPAD-COF	—	1.42	18
DPPT-1 COF	Cellulose membrane	3.45	19
PT-COF	Wood	2.07	20
TpPa-SO_3H-COF	Graphene	3.69	21
DPP-TPA COF	Polyvinyl alcohol	2.5	22
USTB-39-M	Chitosan	3.42	23
UCOF-366-OH	Polyvinylidene fluoride	2.51	24
STTP COF	—	3.55	25
NKCOF-47	—	3.02	26
CTF-tertA	Carbon nanotube	1.59	27
BTz-COF-T	Cellulose	3.60	This work

Supporting references

(1) Lu, T.; Chen, F. Multiwfn: A multifunctional wavefunction analyzer. *J. Comput. Chem.* **2012**, *33* (5), 580-592.

(2) Hou, H.; Wu, K.; Chen, X.; Liu, X.; Zhao, Y. Thiazole-bimodulated covalent organic frameworks for synergistic water harvesting and photosplitting. *J. Am. Chem. Soc.* **2025**, *147* (31), 27835-27846.

(3) Wang, Y.; Zhao, P.; Zhang, Y.; Liu, S.; Mao, S.; Chen, W.; Guo, P.; Min, L.; Feng, R.; Li, X. All-day multifunction hygroscopic salt/aerogels/photocatalysts system for efficient freshwater-hydrogen-oxygen co-production from air. *Sci. China Chem.* **2025,** 68, 4785-4795.

(4) Li, J.; Ding, L.; Su, Z.; Li, K.; Fang, F.; Sun, R.; Qin, Y.; Chang, K. Non-lignin constructing the gas–solid interface for enhancing the photothermal catalytic water vapor splitting. *Adv. Mater.* **2023**, *35* (45), 2305535.

(5) He, L.; Zeng, X.; Chen, H.; Zhao, L.; Huang, Z.; Wang, D.; He, X.; Fang, W.; Du, X.; Li, W. A Hybrid photocatalytic system splits atmospheric water to produce hydrogen. *Adv. Funct. Mater.* **2024**, *34* (19), 2313058.

(6) Zeng, C.-h.; Xie, S.; Yu, M.; Yang, Y.; Lu, X.; Tong, Y. Facile synthesis of large-area CeO_2/ZnO nanotube arrays for enhanced photocatalytic hydrogen evolution. *J. Power Sources* **2014**, *247*, 545-550.

(7) Ma, N.; Dong, L.; Zhang, T.; Xie, N. e.; Tian, L.; Zhang, Z.; Guan, X.; Guo, L. A photothermal-photocatalytic layered aerogel for harvesting water and hydrogen from seawater. *J. Colloid Interface Sci.* **2025**, *687*, 573-581.

(8) Rao Pala, L. P.; Peela, N. R. Green hydrogen production in an optofluidic planar microreactor via photocatalytic water splitting under visible/simulated sunlight irradiation. *Energy Fuels* **2021**, *35* (23), 19737-19747.

(9) Lu, J.; Hu, H.; Yang, S.; Shanmugam, P.; Wei, W.; Selvaraj, M.; Xie, J. ZnS@carbonaceous aerogel composites fabricated in production of hydrogen and for removal of organic pollutants. *J. Mater. Sci.: Mater. Electron* **2018**, *29* (10), 8523-8534.

(10) Cui, A.; Wang, Y.; Liu, Z.; Jiang, X.; Liu, D.; Lu, C.; Wang, X.; Liang, R.; Huang,

L.; He, X.; et al. Sub-minute synthesis of nano-COFs as highly efficient photocatalysts for enhanced H_2 evolution in seawater. *Appl. Catal. B: Environ Energy* **2026**, *380*, 125785.

(11) Yue, Q.; Zhang, Z.; Liu, X.; Zhu, C.; Wen, Y.; Fu, P.; Hu, Q.; Qu, X.; Zhou, Y.; Wang, J. Engineering electron delocalization of ultrathin covalent organic framework nanosheets to elevate photocatalytic hydrogen evolution in seawater. *Chem. Eng. J.* **2025**, *507*, 160481.

(12) Shi, Y.; Chen, Z.; Hao, P.; Shan, P.; Lu, J.; Guo, F.; Shi, W. Boosting photothermal-assisted photocatalytic water/seawater splitting into hydrogen based on greenhouse-induced photothermal effect. *J. Colloid Interface Sci.* **2024**, *653*, 1339-1347.

(13) Yang, C.; Qin, J.; Rajendran, S.; Zhang, X.; Liu, R. WS_2 and C-TiO_2 nanorods acting as effective charge separators on *g*-C_3N_4 to boost visible-light activated hydrogen production from seawater. *ChemSusChem* **2018**, *11* (23), 4077-4085.

(14) Zhu, C.; Liu, C. a.; Fu, Y.; Gao, J.; Huang, H.; Liu, Y.; Kang, Z. Construction of CDs/CdS photocatalysts for stable and efficient hydrogen production in water and seawater. *Appl. Catal. B* **2019**, *242*, 178-185.

(15) Zhang, Y.; Niu, L.; Li, Z.; Yang, T.; Liu, Y.; Kang, Z. A recyclable $ZnIn_2S_4$/PAN photocatalytic nanofiber membrane for boosting visible light hydrogen evolution in seawater without cocatalyst. *Appl. Catal. B: Environ Energy* **2024**, *357*, 124300.

(16) Lu, J.; Shi, Y.; Chen, Z.; Sun, X.; Yuan, H.; Guo, F.; Shi, W. Photothermal effect of carbon dots for boosted photothermal-assisted photocatalytic water/seawater splitting into hydrogen. *Chem. Eng. J.* **2023**, *453*, 139834.

(17) Liu, Y.; Xiang, Z. Fully conjugated covalent organic polymer with carbon-encapsulated Ni_2P for highly sustained photocatalytic H_2 production from seawater. *ACS Appl. Mater. Interfaces* **2019**, *11* (44), 41313-41320.

(18) Yan, X.; Lyu, S.; Xu, X.-Q.; Chen, W.; Shang, P.; Yang, Z.; Zhang, G.; Chen, W.; Wang, Y.; Chen, L. Superhydrophilic 2D covalent organic frameworks as broadband absorbers for efficient solar steam generation. *Angew. Chem. Int. Ed.* **2022**, *61* (19), e202201900.

(19) Sun, S.-X.; Huang, Z.-H.; Wang, Z.-F.; Xu, D.-X.; Jiang, C.-C.; Xu, J.-W. Size modulation of covalent organic frameworks for enhanced solar-driven photothermal evaporation efficiency. *Small* **2025**, *21*, e08677.

(20) Zhang, R.-W.; Huang, Q.; Zhang, J.; Zhao, Y.-J.; Zhou, H.; Wu, T.; Ji, R.; Wu, P.; Tian, D. Photothermal-photocatalysis system by photosensitive covalent organic framework@wood for efficient solar-driven water evaporation and uranium removal. *Adv. Funct. Mater.* **2025**, e15344.

(21) Li, C.; Cao, S.; Lutzki, J.; Yang, J.; Konegger, T.; Kleitz, F.; Thomas, A. A covalent organic framework/graphene dual-region hydrogel for enhanced solar-driven water generation. *J. Am. Chem. Soc.* **2022**, *144* (7), 3083-3090.

(22) Huang, Z.; Luo, Y.-H.; Geng, W.-Y.; Wan, Y.; Li, S.; Lee, C.-S. Marriage of 2D covalent–organic framework and 3D network as stable solar-thermal still for efficient solar steam generation. *Small Methods* **2021**, *5* (5), 2100036.

(23) Lu, X.; Fang, X.; Jin, Y.; Wang, H.; Li, X.; Xie, Y.; Jiang, J. High-efficiency interfacial solar steam generation by metallophthalocyanine COFs coated on hydrogels. *Chem. Eng. J.* **2025**, *508*, 161018.

(24) Lu, Q.; Zhao, X.; Jiang, Y.; Zhao, K.; Pan, J. Nano-structured urchin-like photothermal covalent organic frameworks for efficient solar-driven interfacial water evaporation. *Chem. Eng. J.* **2024**, *499*, 156308.

(25) Li, G.; Yue, Q.; Fu, P.; Wang, K.; Zhou, Y.; Wang, J. Ionic dye based covalent organic frameworks for photothermal water evaporation. *Adv. Funct. Mater.* **2023**, *33* (34), 2213810.

(26) Jia, S.; Hao, L.; Liu, Y.; Lin, E.; Liu, W.; Yang, Y.; Tian, Y.; Peng, Y.; Cheng, P.; Chen, Y.; et al. Freestanding hydrophilic/hydrophobic janus covalent organic framework membranes for highly efficient solar steam generation. *ACS Mater. Lett.* **2023**, *5* (2), 458-465.

(27) Guo, L.; Gong, J.; Song, C.; Zhao, Y.; Tan, B.; Zhao, Q.; Jin, S. Donor–Acceptor charge migration system of superhydrophilic covalent triazine framework and carbon nanotube toward high performance solar thermal conversion. *ACS Energy Lett.* **2020**, *5* (4), 1300-1306.